

Topological Phenomena in Trapped Ion Systems

T. Shi and J. I. Cirac

Max-Planck-Institut für Quantenoptik, Hans-Kopfermann-Strasse 1, Garching, Germany

(Dated: July 29, 2021)

We propose and analyze a scheme to observe topological phenomena with ions in microtraps. We consider a set of trapped ions forming a regular structure in two spatial dimensions and interacting with lasers. We find phonon bands with non-trivial topological properties, which are caused by the breaking of time reversal symmetry induced by the lasers. We investigate the appearance of edge modes, as well as their robustness against perturbations. Long-range hopping of phonons caused by the Coulomb interaction gives rise to flat bands which, together with induced phonon-phonon interactions, can be used to produce and explore strongly correlated states. Furthermore, some of these ideas can also be implemented with cold atoms in optical lattices.

PACS numbers: 37.10.Ty, 37.10.Vz, 05.30.Jp, 11.30.Er

I. INTRODUCTION

Atomic systems have revealed themselves as ideal laboratories to study many-body quantum systems. Atoms or molecules in optical lattices [1, 2] realize Hubbard models, both bosonic [3] and fermionic [4], and thus can be used to study some of the most basic models of electron transport and magnetism appearing in condensed matter physics. Starting from the seminal experiment [5], many groups are now able to implement different versions of Hubbard-like models. Although at the moment the temperatures in most of those experiments are too high, single site addressing [6, 7] and other techniques are currently opening up new avenues for the observation of many new and exciting phenomena. Trapped ions can also realize bosonic Hubbard models [8], as well as many other spin models [9, 10]. Despite recent experimental breakthroughs [11], ions are not yet as versatile as atoms in lattices. However, this situation may soon change with the development of surface traps [12–16] or through the combination of ions and optical lattices [17].

One of the goals of atomic experiments is the simulation of the Fractional Quantum Hall Effect (FQHE), one of the most celebrated discoveries in condensed matter physics. In the standard electronic scenario, it appears at very low temperatures in the presence of both an external magnetic field and strong interactions. The first restricts the electron motion to the first Landau level, whereas the latter is responsible for the generation of strong correlations. It has recently been suggested that, under some conditions, in lattice systems a similar behavior should occur even in the absence of a net magnetic flux [18, 19]. The first condition is that the band structure should possess a non-trivial topology, as characterized by the so-called Chern Number (CN). The second one is that the width of the band should be much smaller than the band gap, i.e., one has flat bands, something which is associated to hopping beyond nearest neighboring sites. In such a situation, the lattice problem resembles the standard scenario for the appearance of the FQHE, whereby the flat band plays the role of the first Landau level. In-

teraction energies larger than single particle ones should thus give rise to strongly correlated states at low temperatures and, in particular, to states displaying fractionalization as well as to anyonic excitations.

Even in the absence of interactions, the non-trivial topology of the energy bands gives rise to very intriguing behavior. In particular, when we consider a problem with open boundary conditions (as opposed to periodic boundary conditions) new energies appear within the band gap in the spectrum, with a nearly linear dispersion relation. The corresponding modes are located at the boundary of the system, and thus those are called “edge modes” [20]. The presence of those modes is presumably very robust against perturbations [21, 22].

In atomic systems, in the bulk, one can simulate the action of a magnetic field either by rotating the trap holding the atoms [23] or by using laser fields [24–26]. In optical lattices, a very promising alternative consists of using complex hopping amplitudes induced by the lasers [27] (see also [26]). The appearance of FQHE-like behavior in optical lattices was first considered by Hafezi et al [28] in the low density limit, where the lattice does not play an important role. In addition, they proposed to use dipole-dipole interactions to increase the band gap (see also [22, 29–31]), and thus be able to increase the density. In a recent paper, an implementation based on polar molecules [32] is proposed which achieves very flat bands by exploiting the dipole-dipole interaction among them, and thus is very well suited for the observation of the FQHE.

In this paper we show that trapped ions can be used to investigate some of the intriguing features mentioned above. We consider ions in microtraps, forming a regular structure in two spatial dimensions. They are driven by lasers, which are far off resonance with respect to an internal electronic transition. By carefully choosing the laser configuration, the ions experience a force that breaks the time-reversal symmetry. Furthermore, phonons (i.e., motional quanta in each of the ions) can hop from one ion to another due to the Coulomb interaction, which has a long range. As a result of all that,

we find a band structure with a non-trivial topological structure, as witnessed by the corresponding CN. We investigate the appearance of edge modes, as well as their fragility in the presence of perturbations. We also study the regime of parameters where the bands are very flat, whereby FQHE-like behavior could be investigated by adding phonon-phonon interactions as proposed in [8]. Note that other methods to obtain flat bands (albeit without topological properties) have been recently proposed for trapped ions using time-dependent gadgets [33]. We emphasize that the scheme presented here is quite different from the one proposed for atoms in optical lattices, as here the hopping terms are all real, whereas the on-site Hamiltonian is the one that breaks the time-reversal symmetry. In fact, our scheme resembles more that studied in the context of photonic edge modes [34]. The configuration we propose here could also be suitable in setups involving atoms in optical lattices.

This paper is organized as follows: In Sec. II, we introduce the model setup and derive an effective Hamiltonian for the phonons. In Sec. III, we analyze the energy spectra of the system with toroidal, cylindrical, and planar geometries. In particular, we derive the CN for the different bands and relate them to the appearance of edge modes. In Sec. IV, we propose a scheme to detect the edge modes by using a periodically driven electric field that shakes the ion lattice. In Sec. V, we discuss that, due to the flat lowest band, phonon-phonon interactions could lead to the observation of a bosonic version of the FQHE. Some of the details of the derivations are presented in the appendices.

II. MODEL SETUP

We consider N ions confined in microtraps and interacting with lasers in a planar geometry. The lasers are tuned far off-resonance with respect to any optical transition, so that the ion stays most of the time in its ground electronic internal state. Virtual transitions mediated by the lasers modify the atomic motion. In particular, they give rise to a Doppler effect which, when combined with dipole forces, generates something that resembles the Lorenz force produced by a magnetic field. This force, which breaks the time-reversal symmetry of the problem, is one of the main ingredients required for the appearance of the topological features which we are looking after. The other one is the Coulomb interaction among the ions, which allows phonons to move from ion to ion [8]. The effective dynamics of the phonons in the ion lattice are described by a Hamiltonian which breaks time-reversal symmetry and, as we will see, has the desired topological properties.

There are many lattice geometries that give rise to topological features. Here, for the sake of concreteness, we will consider a hexagonal (honeycomb) geometry [see Fig.1(a)]. In this section we will first introduce the interaction of the laser with each ion, and derive the cor-

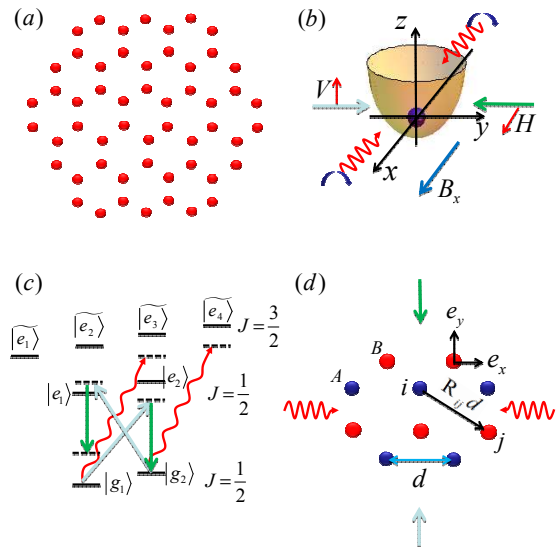


FIG. 1: (Color online) Configuration: (a) Ions are trapped in microtraps forming a planar hexagonal geometry. (b) Laser and magnetic field configuration for each ion in a microtrap. There is a homogenous magnetic field as well as a laser standing-wave with circular polarization along the x direction, and two counter-propagating lasers in lin⊥lin configuration along the y direction. (c) Ion internal structure, where the quantization axis is chosen along the magnetic field (x axis). For simplicity, we consider no nuclear spin (hyperfine structure). The magnetic field generates a Zeeman shift. The lasers propagating along the x direction (in red) produce different AC-Stark shifts on the magnetic levels. Lasers along the y direction induce Raman transitions. (d) Detail of the hexagonal lattice, with the unit vectors $e_{x,y}$ indicating the two oscillation directions of the ions (vibrational modes). Different colors are used for the A and B sublattices.

responding Lorenz-like force. Some of the details regarding a particular laser configuration that implements those forces are given in Appendix A. Later on, we will consider the interaction among the ions in order to derive the effective Hamiltonian describing the phonon dynamics.

A. Single-ion dynamics

Let us first consider a single ion, as shown in Fig. 1b, with two electronic (internal) ground levels $|g_{1,2}\rangle$ interacting with lasers. The single-ion Hamiltonian contains three parts: $H_{si} = H_{HO} + H_x^{\text{las}} + H_y^{\text{las}}$ where ($\hbar = 1$)

$$\begin{aligned}
 H_{HO} &= \sum_{\alpha=x,y} \left(\frac{p_{\alpha}^2}{2M} + \frac{1}{2} M \omega_{\alpha}^2 r_{\alpha}^2 \right), \\
 H_x^{\text{las}} &= \Omega_x K r_x \sigma_z, \\
 H_y^{\text{las}} &= \frac{\Omega_y}{2} (e^{iK r_y} \sigma^+ + \text{H.c.}), \quad (1)
 \end{aligned}$$

Here, H_{HO} describes the harmonic oscillation of the ion in the plane, where M is the mass, and r_α , p_α , and ω_α denote the position and momentum operators, and the trap frequency along the direction α , respectively. The terms $H_{x,y}^{\text{las}}$ describe internal level-dependent dipole and radiation pressure forces, respectively. Here K is twice the wavevector of the lasers, $\Omega_{x,y}$ the effective Rabi frequencies, $\sigma_z = |g_2\rangle\langle g_2| - |g_1\rangle\langle g_1|$, and $\sigma^+ = |g_2\rangle\langle g_1|$.

Hamiltonian (1) can be implemented in different ways. One possible one is depicted in Fig. 1(b,c), which uses a magnetic field along the x direction, and two pairs of far off-resonant counterpropagating beams along the x and y direction. In Appendix A we give the details of this scheme, as well as how to obtain H_{si} after the adiabatic elimination of the excited states.

It is convenient to transform the Hamiltonian (1) according to the unitary operator $U = \exp(iKr_y\sigma_z/2)$

$$\tilde{H}_{\text{si}} = U^\dagger H_{\text{si}} U = H_{\text{HO}} + \frac{\Omega_y}{2}\sigma_x + (\Omega_x Kr_x + \frac{Kp_y}{2M})\sigma_z, \quad (2)$$

where the last term represents the Doppler shift along the y direction and we have used the standard notation $\sigma_x = \sigma^+ + \sigma^-$. In the following we will simplify the model by assuming that $|\Omega_y \pm \omega_\alpha| \gg \Omega_x \eta_x, \omega_y \eta_y$, where $\eta_\alpha = K\ell_\alpha$ are the dimensionless Lamb-Dicke parameters, which are typically ≤ 1 (and $\ell_\alpha = (2M\omega_\alpha)^{-1/2}$ is the ground state size). Assuming that the ion is initially prepared in the state $|\downarrow\rangle = (|g_2\rangle - |g_1\rangle)/\sqrt{2}$, we show in Appendix B that, after the adiabatic elimination of the internal states, one ends up with the effective Hamiltonian

$$H_{\text{eff}} = \bar{H}_{\text{HO}} + \Omega r_x p_y. \quad (3)$$

The position-momentum coupling is characterized by

$$\Omega = - \sum_{\alpha=x,y} \frac{\Omega_x \Omega_y \omega_\alpha \eta_\alpha^2}{\Omega_y^2 - \omega_\alpha^2}, \quad (4)$$

and \bar{H}_{HO} describes harmonic oscillations with renormalized frequencies $\tilde{\omega}_\alpha$ (see Appendix B). This Hamiltonian resembles the one describing the Lorenz force exerted by a magnetic field on a charge (note, however, that it is not invariant under rotations along the z axis).

B. Coulomb Interactions

Let us now consider the whole set of ions. As mentioned above, the microtraps are disposed according to a 2D honeycomb lattice, as shown in Fig. 1(a,d). The interaction of each of the atoms with the lasers is given by (3). Coulomb forces induce repulsion between the ions. Assuming that $d \gg \ell_\alpha$, we can expand the Coulomb interaction up to second order in the displacements $r_\alpha^{(i)}$ about the center of the i -th microtrap, obtaining

$$U_C = \frac{e^2}{2d^3} \sum_{i,j,\alpha\beta} r_\alpha^{(i)} U_{\alpha,\beta}^{i,j} r_\beta^{(j)} \quad (5)$$

where

$$U_{\alpha,\beta}^{i,j} = \begin{cases} \frac{1}{|\mathbf{R}_{ij}|^3} [\mathbf{e}_\alpha \cdot \mathbf{e}_\beta - \frac{3(\mathbf{e}_\alpha \cdot \mathbf{R}_{ij})(\mathbf{e}_\beta \cdot \mathbf{R}_{ij})}{|\mathbf{R}_{ij}|^2}], & i \neq j, \\ \sum_{j' \neq i} \frac{1}{|\mathbf{R}_{ij'}|^3} [\frac{3(\mathbf{e}_\alpha \cdot \mathbf{R}_{ij'})(\mathbf{e}_\beta \cdot \mathbf{R}_{ij'})}{|\mathbf{R}_{ij'}|^2} - \mathbf{e}_\alpha \cdot \mathbf{e}_\beta], & i = j, \end{cases} \quad (6)$$

As shown in Fig. 1d, \mathbf{e}_α are the unit vectors, and $\mathbf{R}_{ij}d$ is the vector pointing from the site i to the site j . We have omitted the linear terms in $r_\alpha^{(i)}$, which just redefine the trap center. Furthermore, the $U_{\alpha,\alpha}^{i,i}$ just shift the frequencies $\tilde{\omega}_\alpha$, and can be absorbed in $\tilde{\omega}_\alpha$.

The complete Hamiltonian, H , consisting of the single-ion terms as well as the Coulomb interaction, can be rewritten in terms of the phonon annihilation operators

$$a_\alpha^{(i)} = \sqrt{\frac{M\tilde{\omega}_\alpha}{2}} r_\alpha^{(i)} + i\sqrt{\frac{1}{2M\tilde{\omega}_\alpha}} p_\alpha^{(i)}. \quad (7)$$

In the stiff limit $\beta_\alpha = e^2/(M\tilde{\omega}_\alpha^2 d^3) \ll 1$, where we can drop the non-phonon number conserving terms [9], and we finally obtain the Hamiltonian for the phonons

$$H = \sum_{ij,\alpha\beta} a_\alpha^{(i)\dagger} \mathcal{H}_{\alpha,\beta}^{i,j} a_\beta^{(j)}. \quad (8)$$

This describes phonon hopping without interaction (i.e., it is quadratic in creation and annihilation operators), and is characterized by the ‘‘single-particle’’ Hamiltonian

$$\frac{\mathcal{H}_{\alpha,\beta}^{i,j}}{\tilde{\omega}_x} = \frac{\beta_x U_{\alpha,\beta}^{i,j}}{2\gamma_\alpha \gamma_\beta} + \delta_{ij} (\delta_{\alpha x} \delta_{\beta x} + \gamma_y^2 \delta_{\alpha y} \delta_{\beta y}) - iV_b \delta_{ij} (\delta_{\alpha x} \delta_{\beta y} - \delta_{\alpha y} \delta_{\beta x}) \quad (9)$$

in terms of the dimensionless parameters β_x , $\gamma_\alpha = \sqrt{\tilde{\omega}_\alpha/\tilde{\omega}_x}$, and $V_b = \Omega\gamma_y/(2\tilde{\omega}_x)$. For the sake of simplicity, in the following we will set $\gamma_\alpha = 1$, so that the problem is fully determined by two parameters. The corresponding values are restricted by the conditions employed in the derivation of the Hamiltonian (9). In particular, $\beta_x \ll 1$, and $|V_b| = \eta^2 \Omega_x / \Omega_y \lesssim \eta$, where we have taken $\eta_x = \eta_y = \eta$. Taking the $^{20}\text{Ca}^+$ ion, $\omega_x = \omega_y = \Omega_x \sim 0.1\text{MHz}$, $\Omega_y \sim 0.3\text{MHz}$, and $d \sim 10\text{-}100\mu\text{m}$, we obtain values for η up to 0.8 [35], $\beta_x \in [0.01, 0.3]$ and $|V_b| \in [0.05, 0.3]$, which are the values that we take in the examples given below.

The last term in Eq. (9) breaks the time-reversal symmetry, which results from the position-momentum coupling. Thus, a non-trivial topological phase may be expected to emerge in this setup.

III. TOPOLOGICAL PROPERTIES

In this section, we study the topological properties of the ion system. For that, we first consider periodic boundary conditions (PBC), i.e., a toroidal geometry, and analyze the spectrum of the Hamiltonian. Given the periodicity of the problem, it has a band structure,

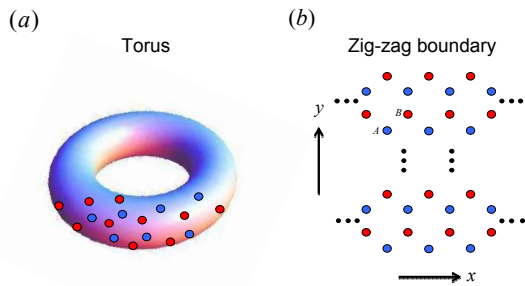


FIG. 2: (Color online) Different configurations considered in the text: (a) torus (PBC); (b) cylinder.

where the existence of a non-trivial topological structure of each band is characterized by the CN [20]. We find that, depending on the values of β_x and V_b , some of the bands exhibit non-zero CN. Then, we consider a cylindrical geometry (i.e. PBC along one direction only). The spectrum is very similar to the one corresponding to the torus, but now new energies appear at the gaps between bands with certain CN configuration. The corresponding eigenmodes (so-called edge modes [20, 36]) appear in pairs, are localized at the two boundaries of the cylinder, and propagate in different directions. Finally, we consider the experimentally relevant situation of full open boundary conditions. In such a case, we also find edge modes. We further investigate their robustness with respect to small random perturbations.

A. Band structure and Chern numbers

In this subsection, we study the topological properties of the system with PBC, namely, the system has translational invariance along both x and y directions [see Fig. 2(a)]. In order to find the single-particle spectrum of H (i.e. that of \mathcal{H}) we use the Fourier modes, and thus diagonalize

$$\tilde{\mathcal{H}}_{\alpha,\beta}(\mathbf{k}) = \frac{1}{N} \sum_{i,j} \mathcal{H}_{\alpha,\beta}^{i,j} e^{-i\mathbf{k}\cdot\mathbf{R}_{i,j}}, \quad (10)$$

where N is the number of sites and $\mathbf{k} = (k_x, k_y)$ is the two-component quasimomentum in the first Brillouin zone (BZ).

The energy spectrum of $\tilde{\mathcal{H}}_{\alpha,\beta}(\mathbf{k})$ is shown in Fig. 3 for different parameters β_x and V_b . As one can see in the plot, there are a number of energy bands. For $\beta_x = 0.02$ and $V_b = -0.1$, there is a big gap between the first and the second bands, and a small one between the second and the third bands. For $\beta_x = 0.02$ and $V_b = -0.2$, the gap between the second and the third bands becomes larger, and the gap between the first and the second one remains open. For larger $\beta_x \sim 0.04$ and $V_b = -0.1$, the band structure remains the same. However, for $\beta_x \sim 0.04$

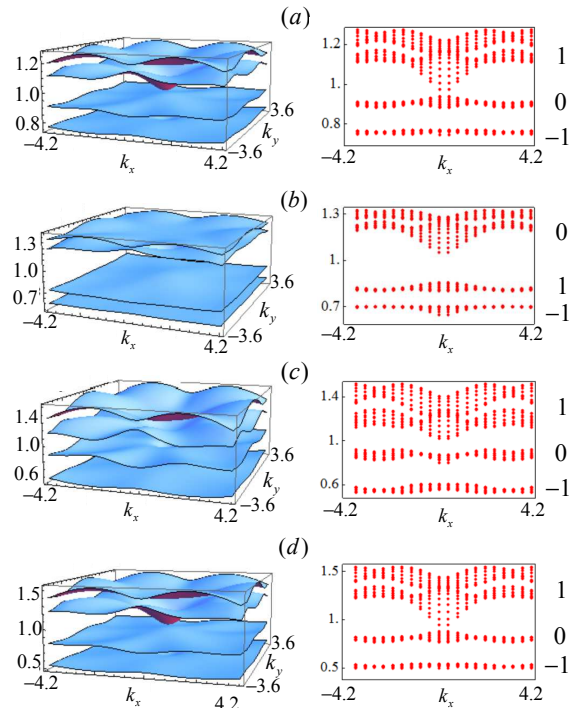


FIG. 3: (Color online) Single-particle energy spectra in units of $\tilde{\omega}_x$ for the system with PBC and $N = 400$. The left panels show the energy spectra as a function of the quasimomenta k_x and k_y (in the first Brillouin zone), whereas the right panels display the same spectra but as a function of k_x only, in order to highlight the different bands and the corresponding gaps. The Chern numbers of each band are shown to the right of such plots. (a) $\beta_x = 0.02$ and $V_b = -0.1$; (b) $\beta_x = 0.02$ and $V_b = -0.2$; (c) $\beta_x = 0.04$ and $V_b = -0.1$; (d) $\beta_x = 0.04$ and $V_b = -0.2$.

and $V_b = -0.2$, the gap between the second and the third bands becomes closed, whereas that between the first and the second band remains.

The topological properties of each band, s , are characterized by the CN, which is defined in terms of the eigenmodes of \mathcal{H} , $|s, \mathbf{k}\rangle$, in the limit $N \rightarrow \infty$ as [20]

$$C_s = \int_{\text{BZ}} \frac{d^2k}{2\pi} \nabla_{\mathbf{k}} \times \mathcal{A}_{\mathbf{k},s}. \quad (11)$$

Here, the integration is taken over quasimomenta in the first BZ, and $\mathcal{A}_{\mathbf{k}} = -i \langle s, \mathbf{k} | \partial_{\mathbf{k},s} | s, \mathbf{k} \rangle$. The CN can be interpreted as the Berry phase obtained if we change adiabatically the quasimomentum cyclically along the boundary of the BZ [37]. Alternatively, if we interpret $\mathcal{A}_{\mathbf{k}}$ as a vector potential, the C is nothing but the total number of magnetic fluxes through the whole BZ. Because the Brillouin zone forms a closed surface, this number (and thus the CN) must be an integer, as it is required by the single-valuedness of gauge transformations [38].

Given that the CN is an integer, we do not need to calculate it for $N \rightarrow \infty$, but a finite N can already give us its value with very high confidence. In general, however,

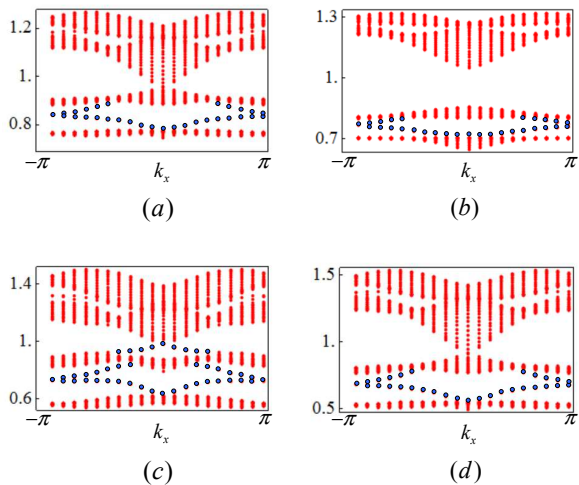


FIG. 4: (Color online) As in Fig.3 for the cylinder geometry and $N = 400$: (a) $\beta_x = 0.02$ and $V_b = -0.1$; (b) $\beta_x = 0.02$ and $V_b = -0.2$; (c) $\beta_x = 0.04$ and $V_b = -0.1$; (d) $\beta_x = 0.04$ and $V_b = -0.2$. The edge modes are marked in blue.

it is very hard to determine the CN through Eq. (11) numerically, since $\mathcal{A}_{\mathbf{k}}$ contains singularities as long as $C \neq 0$. Thus, we use the alternative expression [39]

$$\tilde{C}_s = \text{Im} \int d^2k \sum_{s_1 < s < s_2} \frac{(\partial_{k_x} \mathcal{H}_{\mathbf{k}})_{s_1, s_2} (\partial_{k_y} \mathcal{H}_{\mathbf{k}})_{s_2, s_1}}{\pi (E_{\mathbf{k}, s_1} - E_{\mathbf{k}, s_2})^2}, \quad (12)$$

where $s_i = 1, 2, \dots$ denote the bands from the bottom to the top, $(\partial_{k_i} \mathcal{H}_{\mathbf{k}})_{s_1, s_2} = \langle s_1, \mathbf{k} | \partial_{k_i} \mathcal{H}_{\mathbf{k}} | s_2, \mathbf{k} \rangle$, and $E_{\mathbf{k}, s_i}$ is the energy corresponding to $|s_i, \mathbf{k}\rangle$. Starting from \tilde{C}_s , we can recover the CN using

$$\tilde{C} = \sum_{s'=1}^s C_{s'}. \quad (13)$$

We have determined the CN of the three bands appearing in 3. For a given β_x , as $|V_b|$ increases, the CN of the first, second and third bands vary from $(-1, 0, 1)$ to $(-1, 1, 0)$. A non-zero CN indicates the presence of a non-trivial topological property in the system which, as we will see in the next subsection, is reflected in the appearance of edge modes.

B. Edge modes

Based on the non-vanishing CN found in the previous section, we expect the emergence of edge modes in the boundaries of our system. In this subsection, we focus on those modes for two different geometries: cylinder [2(b)](where there are PBC along the x -direction only), and plane [1(a)].

For a cylindrical geometry, the translational invariance along the y direction is broken. Still, given the periodicity

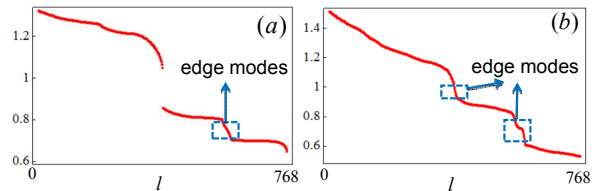


FIG. 5: (Color online) As in Fig.3 for the planar geometry and 384 sites: (a) $\beta_x = 0.02$ and $V_b = -0.2$; (b) $\beta_x = 0.04$ and $V_b = -0.1$. Here, l denotes the eigenmode. Note that for 384 sites, there are 768 eigenmodes.

along x , we can use quasimomenta in this direction, and thus consider the single-particle Hamiltonian

$$\tilde{\mathcal{H}}_{\alpha, \beta}^{i_y, j_y}(k_x) = \frac{1}{N_x} \sum_{i_x, j_x} \mathcal{H}_{\alpha, \beta}^{i, j} e^{-ik_x(i_x - j_x)}, \quad (14)$$

where $i_{x,y}$ denote the x and y coordinates of ion i , $k_x = 2\pi n/N_x$ with $n \leq N_x$ integer, and N_x are the number of sites in a row. By numerical diagonalizing $\tilde{\mathcal{H}}_{\alpha, \beta}^{i_y, j_y}(k_x)$ for each value of k_x we obtain the energy spectra shown in Fig. 4. They are to be compared with those of Fig. 3. We choose two typical examples to explain the relation between the CN and the edge modes. We first consider $\beta_x = 0.02$ and $V_b = -0.2$. The corresponding spectra are shown in Fig. 3(b) and Fig. 4(b), respectively. As explained in the previous section, the CN for the first, second, and third bands are $-1, 1, 0$, respectively. Thus, in the cylinder, two edge modes located in the up- and bottom- boundaries emerge in the first band gap. They are signaled by the blue dots that display a nearly linear dispersion relation with opposite slopes, which indicate that they are counter-propagating. If we inspect the band gap between the second and the third band, we see that no edge modes show up. The reason is that total CN of the first and the second bands (i.e., its sum) is zero. The second example is for $\beta_x = 0.04$ and $V_b = -0.1$ [Fig. 4(c)]. Here, the CN for the first, second, and third bands are $-1, 0, 1$, respectively. Therefore, in each band gap there are two counter-propagating edge modes.

For the planar geometry, the translational invariance is completely broken. By numerical diagonalizing the Hamiltonian \mathcal{H} ,

$$\sum_{j, \beta} \mathcal{H}_{\alpha, \beta}^{i, j} u_{j, \beta}^l = E_l u_{i, \alpha}^l. \quad (15)$$

we obtain the spectra of Fig. 5 and the corresponding eigenmodes, u^l . As shown in Fig. 5(a), for $\beta_x = 0.02$ and $V_b = -0.2$, a set of edge modes emerges in the (small) first band gap, while in the large second band gap there are none. Figure 5(b) shows that edge modes emerge in both the first and second band gap for $\beta_x = 0.04$ and $V_b = -0.1$. Again, these results can be understood in terms of the CN corresponding to the three bands.

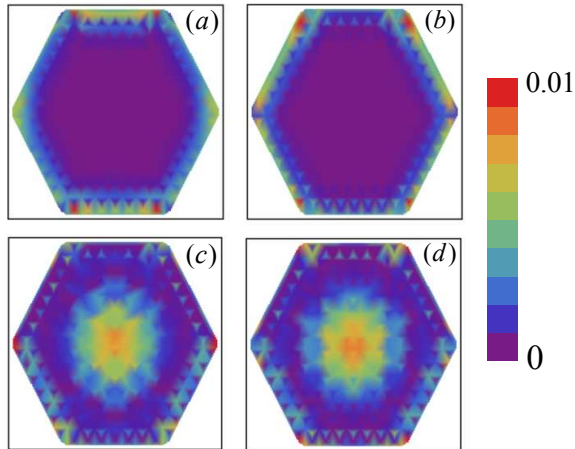


FIG. 6: (Color online) Spatial distribution for typical edge and bulk eigenmodes corresponding to the system with planar geometry, with 384 sites, $\beta_x = 0.04$ and $V_b = -0.1$. (a,c) For an energy $E = 0.7\tilde{\omega}_x$, corresponding to an edge mode and (c,d) $E = 0.9\tilde{\omega}_x$, corresponding to a bulk mode; (a,c) x component (b,d) y component.

In order to verify that those modes are located at the boundaries of our system, we plot in Fig. 6 the spatial distribution of a typical eigenmode corresponding to the edge (a,b) and bulk (c,d). That is, for each ion i , we plot at its location [i.e., at coordinates (i_x, i_y)] the value of $|u_{i,\alpha}^l|^2$ for $\alpha = x$ (a,c) and $\alpha = y$ (b,d).

Edge modes are supposed to be robust against small perturbations (with energy densities smaller than the band gap; or, strictly speaking, as long as the gap does not close) [21]. One can understand this behavior in a simple way by resorting to the cylindrical geometry. There, impurities (or perturbations) cannot back-scatter the propagation of phonons in one boundary since there are no modes available (they are located in the other boundary of the cylinder). In order to test this robustness, we have introduced random perturbations in the planar geometry. In particular, we have added for each of the ions: (i) to $|V_b|$ a random number in the interval $(0.15, 0.25)$ and to $\tilde{\omega}_x$ a random number in the interval $(0.95, 1.05)$ in Fig. 7(a); (ii) to $|V_b|$ a random number in the interval $(0.05, 0.15)$ and to $\tilde{\omega}_x$ a random number in the interval $(0.95, 1.05)$ in Fig. 7(b)-(d), which results in a random variation in β_x . As we can see, in Fig. 7(a,b) the energy spectrum still has some energies within the band gap, and the corresponding modes are located at the boundary [Fig. 7(c,d)]. This confirms that the edge modes are well-protected and robust.

IV. PROBING THE EDGE MODES

In this section, we propose a method to detect the edge modes. Since the ions are charged, they can respond to

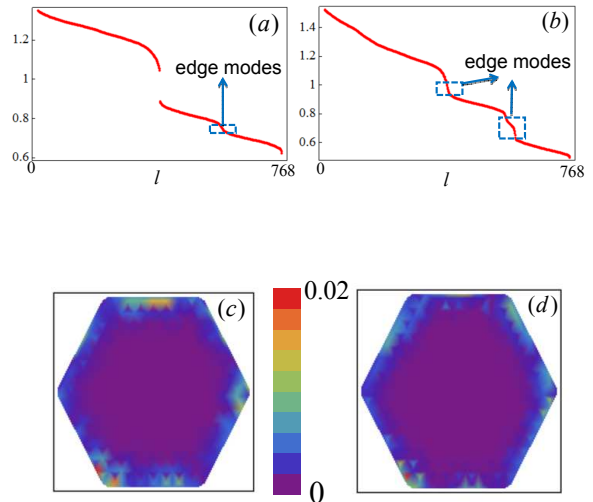


FIG. 7: (Color online) Single particle spectra in units of $\tilde{\omega}_x$ (a,b) and the spatial distribution for the x and y components (c,d) of an eigenmode with energy $E = 0.7\tilde{\omega}_x$ for a planar geometry with 384 lattice sites. We have added to the values V_b and β_x random numbers as explained in the main text.

an external electric field. We consider a periodic electric field that shakes the lattice along the x -direction with frequency ω_d . If we initially prepare the ions in the motional ground state (i.e., the state with no phonons), phonons will be generated by the electric field. After a time t_f , the field is turned off. As we will show below, if the frequency ω_d is chosen to be the one corresponding to the edge modes in the spectrum, phonons will be generated at the boundary of the system, indicating the presence of edge modes at that frequency. The presence of phonons can be detected using standard ion trap techniques [40, 41].

The interaction between the ions and the electric field reads

$$H_p(t) = \sum_j F_j r_x^{(j)} \cos(\omega_d t), \quad (16)$$

where F_j is the force driving the ion at site j . We define the density distribution of the x -phonon at time t as $\rho_j(t) = \langle 0 | a_x^{(j)\dagger}(t) a_x^{(j)}(t) | 0 \rangle$. Here, $|0\rangle$ is the (vacuum) state with no phonons, and $a_x^{(j)}(t)$ denote the operators in the Heisenberg picture. By solving the Heisenberg equations of motion, we obtain

$$\rho_j(t) = \frac{1}{4} \left| \sum_{l,m=\pm 1} u_{j,x}^l f_l^* \frac{e^{-iE_l t} - e^{im\omega_d t}}{E_l + m\omega_d} \right|^2, \quad (17)$$

where $f_l = \sum_j \Omega_j u_{j,x}^l$ is the effective driving force corresponding to the eigenmode l , $\Omega_j = F_j / \sqrt{2M\tilde{\omega}_x}$.

In Fig. 8, we plot the normalized phonon density distribution

$$\bar{\rho}_j(t_{\text{final}}) = \frac{\rho_j(t_{\text{final}})}{\sum_j \rho_j(t_{\text{final}})} \quad (18)$$

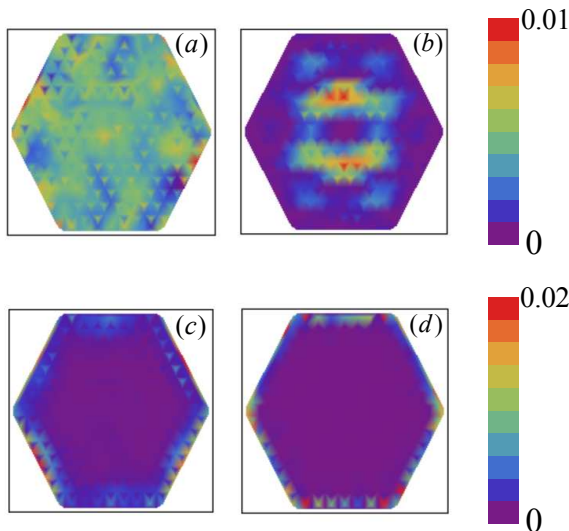


FIG. 8: (Color online) Density distribution of x -phonons after the evolution time t_f for $\beta_x = 0.04$ and $V_b = -0.1$: (a) $\omega_d = 2.0\tilde{\omega}_x$; (b) $\omega_d = 0.6\tilde{\omega}_x$; (c) $\omega_d = 1.0\tilde{\omega}_x$; (d) $\omega_d = 0.7\tilde{\omega}_x$.

for different driving frequencies ω_d at time $t_f = 1000/\tilde{\omega}_x$. Here, we have considered the simplest case, namely, $\Omega_j = \Omega_0$, the same for all ions. In Fig. 8(a), the driving frequency $\omega_d = 2.0\tilde{\omega}_x$ lies outside the whole energy bands, and thus no resonance occurs, which results in a weak phonon excitation. When the driving frequency $\omega_d = 0.6\tilde{\omega}_x$ is on resonance with one of the bulk states, many phonons are generated in the bulk, as shown in Fig. 8(b). For driving frequencies $\omega_d = \tilde{\omega}_x$ and $0.7\tilde{\omega}_x$ some of the edge modes become resonant, and thus the density of phonons in the boundary is much larger than that in the bulk, which indicates the presence of an edge mode.

V. PHONON-PHONON INTERACTION

As we showed in previous sections, with trapped ions it should be possible to obtain bands in the spectrum with non trivial CN. Furthermore, due to the nature of Coulomb interactions, phonons can hop over long distances, which may give rise to flat bands. Thus, by engineering interactions among the phonons one should be able to induce strong correlations and investigate phenomena like fractionalization with this bosonic system. In this section we will analyze the flatness of the bands for the model introduced in Sec. II, as well as how to induce interactions among the phonons.

The flatness, F , of a band can be characterized by the ratio between the band gap and the bandwidth. In Fig. 9(a) we have plotted F as a function of V_b and β_x for the first band which has CN -1 . This figure shows that values of the order of 10 can be reached within our setup. Those values should be large enough to allow for the investigation of strong correlation effects with this system.

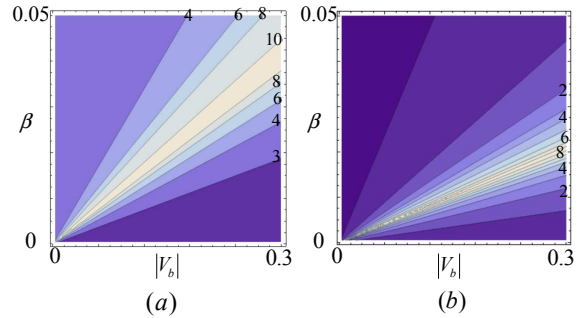


FIG. 9: (Color online) (a) Flatness F of the first band as a function of V_b and β_x . (b) Same for a model where phonon hopping is restricted to nearest neighbors.

In Fig. 9(b) we plot F for the same model as the one considered here, but where phonon hopping is (artificially) restricted to nearest neighbors. As one can see, the flatness of the band becomes smaller than in the previous case, indicating that the long range hopping present in the ion trap system helps to flatten the band. Note that the model with NN hopping could be implemented using atoms in optical lattices and, despite the fact that the flatness is smaller, it may lead to interesting regimes for that system.

In Ref. [8] it was shown how a laser can induce phonon-phonon interactions in the context of the Hubbard model. One can use the same idea in our setup. In particular, in Appendix C we show how to implement the interaction Hamiltonian

$$H_U = U_{\text{int}} \sum_j a_x^{(j)\dagger 2} a_x^{(j)2}, \quad (19)$$

where U_{int} is determined by the Rabi frequency of the standing wave and the Lamb-Dicke parameter. In order to enter the interesting regime of strong correlations, the parameter U_{int} should be smaller than the band gap, so that the interactions do not mix bands. However, it should be larger than the bandwidth, so that the interactions dominate over single phonon dynamics. Taking $\tilde{\omega}_x = 0.1\text{MHz}$, $\beta_x = 0.04$ and $V_b = -0.2$, Fig. 3(d) shows that $U_{\text{int}} \simeq 10\text{KHz}$ should fulfill the conditions to obtain strong correlations.

VI. CONCLUSIONS AND OUTLOOK

In this paper, we have proposed a scheme to induce topological effects in a system of ions trapped in microtraps. The main idea is to use laser fields that break time-reversal symmetry. In particular, we have considered a pair of counterpropagating lasers which are coupled to the position and momentum of the ions, respectively, giving rise to a Lorenz-like force. This coupling is very similar in spirit to the one proposed and used in neutral atom systems. In a honeycomb lattice, one obtains

a band structure with non-trivial CN, which give rise to edge modes. We have analyzed the robustness of such modes against small perturbations, an proposed a way for detecting them. We have also studied the flatness of the bands, and show how to induce phonon-phonon interactions. Our results indicate that as soon as microtraps are available, they should be very well suited to investigate the physics of the FQHE with them. We also emphasize that the setup used here to induce the Lorenz-like force could be also used in the context of atoms in optical lattices.

Acknowledgments

This project has been supported by the EU under the IP project AQUITE.

Appendix A: Physical Implementation

In this appendix, we analyze a possible implementation of our model (1). We consider a single earth alkali ion in a microtrap, in the presence of a homogeneous magnetic field along the x direction, as shown in Fig. 1. For simplicity, we ignore the nuclear spin, so that the ion has two electronic ground state levels, $|g_n\rangle$ ($n = 1, 2$), and two sets of excited levels, $|e_n\rangle$ ($n = 1, 2$), and $|\tilde{e}_n\rangle$ ($n = 1, \dots, 4$), corresponding to the fine splitting. We have chosen the quantization axis along the direction of the magnetic field (x -direction); so, for instance, $|g_{1,2}\rangle = |J = 1/2, m_J = \mp 1/2\rangle_x$. We set the energy of the ground states as 0 and ω_Z (Zeeman splitting), and that of the excited states as ω_n , and $\tilde{\omega}_n$.

The ions interact with two sets of counterpropagating beams along the x and y directions. The first ones form a standing wave with frequency ω_{sw} and circular polarization σ^+ , so that the electric field is $\mathbf{E}_0 \sin(K_0 x + \phi) \cos(\omega_{\text{sw}} t)$. They induce transitions $|g_1\rangle \leftrightarrow |e_2\rangle$, $|\tilde{e}_3\rangle$, and $|g_2\rangle \leftrightarrow |\tilde{e}_4\rangle$, which are described by the Hamiltonian

$$H_{\text{sw}} = [\Omega_{\tilde{e}_3 g_1}(x) |\tilde{e}_3\rangle \langle g_1| + \Omega_{e_2 g_1}(x) |e_2\rangle \langle g_1| + \Omega_{\tilde{e}_4 g_2}(x) |\tilde{e}_4\rangle \langle g_2| + \text{H.c.}] \cos(\omega_{\text{sw}} t), \quad (\text{A1})$$

where $\Omega_{ij}(x) = \Omega_{ij} \sin(K_0 x + \phi)$, and the Rabi frequencies $\Omega_{ij} = \langle i | \mathbf{d} \cdot \mathbf{E}_0 | j \rangle$ are determined by the amplitude of the electric field and the dipole moment \mathbf{d} of ions, and x is the position operator of the atom in the x direction.

The right-moving laser plane wave (propagating along the y direction) is vertically polarized (along z), has frequency ω_R , and induces transitions $|g_1\rangle \leftrightarrow |e_2\rangle$ and $|g_2\rangle \leftrightarrow |e_1\rangle$, according to

$$H_R = \frac{1}{2} (\Omega_{e_2 g_1}^R |e_2\rangle \langle g_1| + \Omega_{e_1 g_2}^R |e_1\rangle \langle g_2|) e^{iK_0 y - i\omega_R t} + \text{H.c.} \quad (\text{A2})$$

where Ω_{ij}^R are the Rabi frequencies, and y is the position operator of the atom in the y direction. The left-moving plane wave with frequency ω_L and horizontal polarization

(along the x -direction) induces transitions $|g_1\rangle \leftrightarrow |e_1\rangle$ and $|g_2\rangle \leftrightarrow |e_2\rangle$, according to

$$H_L = \frac{1}{2} (\Omega_{e_1 g_1}^L |e_1\rangle \langle g_1| + \Omega_{e_2 g_2}^L |e_2\rangle \langle g_2|) e^{-iK_0 y - i\omega_L t} + \text{H.c.} \quad (\text{A3})$$

Note that we have used that the wavevectors of the standing and travelling waves are approximately the same, K_0 .

In the large detuning limit, where all the detunings are much larger than the Rabi frequencies, by adiabatically eliminating the six higher energy levels, we obtain the effective Hamiltonian

$$H_{\text{inner}} = \sin^2(K_0 x + \phi) (\Delta_1 |g_1\rangle \langle g_1| - \Delta_2 |g_2\rangle \langle g_2|) + \frac{\Omega_y}{2} |g_2\rangle \langle g_1| e^{iK_y y} e^{-i\delta t} + \text{H.c.}, \quad (\text{A4})$$

where $K = 2K_0$, $\Omega_y = \Omega_{e_2 g_2}^{L*} \Omega_{e_2 g_1}^R / [2(\omega_R - \omega_2)]$, and

$$\delta = \omega_R - \omega_Z - \omega_L + \frac{|\Omega_{e_2 g_1}^R|^2 - |\Omega_{e_2 g_2}^L|^2}{4(\omega_R - \omega_2)} \sim \omega_R - (\omega_L + \omega_Z), \quad (\text{A5})$$

such that we can neglect all high-oscillating terms. The AC stark shifts

$$\Delta_1 = \frac{1}{4} \left(\frac{|\Omega_{e_2 g_1}^R|^2}{\omega_{\text{sw}} - \omega_2} - \frac{|\Omega_{\tilde{e}_3 g_1}^L|^2}{\tilde{\omega}_3 - \omega_{\text{sw}}} \right), \quad \Delta_2 = \frac{|\Omega_{\tilde{e}_4 g_2}^L|^2}{4(\tilde{\omega}_4 - \omega_Z - \omega_{\text{sw}})} \quad (\text{A6})$$

can be taken to be the same, i.e., $\Delta_1 = \Delta_2 = \Delta$, if we properly choose the frequency ω_{sw} . Taking the Lamb-Dicke limit, where the ion displacements r_x and r_y along the x and y directions are much smaller than the optical wavelength, and assuming that the trap center coincides with the node of the standing wave ($\phi = -\pi/4$) and $\delta = -\Delta$, the effective Hamiltonian becomes

$$H_{\text{inner}} = \Omega_x K r_x \sigma_z + \frac{\Omega_y}{2} (\sigma^+ e^{iK r_y} + \text{H.c.}) = H_x^{\text{las}} + H_y^{\text{las}}, \quad (\text{A7})$$

where the effective Rabi frequency $\Omega_x = \Delta/2$. Notice that the lattice spacing, d , fulfills $K_0 d = 4\pi n$, where n is an integer. This ensures that each ion experiences the same AC-Stark shift produced by the lasers propagating in the x -direction (cf. H_x^{las}). For the second term, i.e., the Hamiltonian H_y^{las} along y -direction, we replace y by the displacement r_y , since the phase $e^{iK y_0}$ generated by the coordinate y_0 of the equilibrium position can be absorbed into the definition of σ^+ .

Appendix B: Adiabatic elimination of the internal states

In this Appendix, we show the details of the adiabatic elimination of the internal states leading to Eq. (3). Fol-

lowing the Fröhlich transformation [42], we use the generator S to rewrite the Hamiltonian

$$\begin{aligned} H_{\text{eff}} &= e^{-S} \tilde{H}_{\text{single}} e^S \\ &= \tilde{H}_{\text{single}} + [\tilde{H}_{\text{single}}, S] + \frac{1}{2} [[\tilde{H}_{\text{single}}, S], S] + \dots \\ &= H_0 + (H_I + [H_0, S]) + [H_I + \frac{1}{2}[H_0, S], S] \\ &\quad + \frac{1}{2} [[H_I, S], S], \end{aligned} \quad (\text{B1})$$

where $H_0 = H_{\text{HO}} + \Omega_y \sigma_z / 2$ and $H_I = -K(\Omega_x r_x + p_y / 2M) \sigma_x$. In order to make the notation more transparent, we redefine the Pauli spin operators as follows: $\sigma_x \rightarrow \sigma_z$ and $\sigma_z \rightarrow -\sigma_x$. By requiring

$$H_I + [H_0, S] = 0, \quad (\text{B2})$$

we obtain the generator

$$\begin{aligned} S &= \Omega_x \eta_x \left(\frac{a_x \sigma_+}{\Omega_y - \omega_x} + \frac{a_x^\dagger \sigma_+}{\Omega_y + \omega_x} \right) \\ &\quad - i \frac{1}{2} \omega_y \eta_y \left(\frac{a_y \sigma_+}{\Omega_y - \omega_y} - \frac{a_y^\dagger \sigma_+}{\Omega_y + \omega_y} \right) - \text{H.c.} \end{aligned} \quad (\text{B3})$$

Here, $a_{x,y}$ are defined according to Eq. (7). In the limit $|\Omega_y \pm \omega_\alpha| \gg \Omega_x \eta_x, \omega_y \eta_y$, we can keep up to second order in the expansion (B1) and obtain the effective Hamiltonian

$$H_{\text{eff}} = H_0 + \frac{1}{2} [H_I, S]. \quad (\text{B4})$$

In that limit, if initially the internal state is the eigenstate $|\downarrow\rangle_z$ of σ_z , we can project the Hamiltonian H_{eff} onto that eigenstate and obtain

$$H_{\text{eff}} = \frac{p_x^2}{2M} + \frac{1}{2} M \tilde{\omega}_x^2 r_x^2 + \lambda_y \left(\frac{p_y^2}{2M} + \frac{1}{2} M \tilde{\omega}_y^2 r_y^2 \right) + \Omega r_x p_y, \quad (\text{B5})$$

where the renormalized frequencies $\tilde{\omega}_x = \lambda_x \omega_x$ and $\tilde{\omega}_y = \omega_y / \sqrt{\lambda_y}$ are defined by

$$\begin{aligned} \lambda_x &= \sqrt{1 - \frac{2\Omega_y \Omega_x^2 K^2}{M\omega_x^2(\Omega_y^2 - \omega_x^2)}}, \\ \lambda_y &= 1 - \frac{\Omega_y K^2}{2M(\Omega_y^2 - \omega_y^2)}, \end{aligned} \quad (\text{B6})$$

and the position-momentum coupling is

$$\Omega = - \sum_{\alpha=x,y} \frac{\Omega_x \Omega_y K^2}{2M(\Omega_y^2 - \omega_\alpha^2)}. \quad (\text{B7})$$

To be consistent with the adiabatic limit, we can set $\lambda_x \sim \lambda_y \sim 1$.

Appendix C: Induction of phonon-phonon interactions

In this Appendix, we show how one can induce phonon-phonon interactions by using a laser. We basically follow the proposal of [8].

An additional laser standing wave propagating along x -direction with frequency $\tilde{\omega}_{\text{sw}}$ and σ^- polarization induces the transitions $|g_1\rangle \leftrightarrow |\tilde{e}_1\rangle$ and $|g_2\rangle \leftrightarrow |e_1\rangle, |\tilde{e}_2\rangle$. The light-ion interaction is

$$\begin{aligned} H_{\text{int}} &= [\tilde{\Omega}_{\tilde{e}_1 g_1}(x) |\tilde{e}_1\rangle \langle g_1| + \tilde{\Omega}_{e_1 g_2}(x) |e_1\rangle \langle g_2| \\ &\quad + \tilde{\Omega}_{\tilde{e}_2 g_2}(x) |\tilde{e}_2\rangle \langle g_2| + \text{H.c.}] \cos(\tilde{\omega}_{\text{sw}} t), \end{aligned} \quad (\text{C1})$$

where the Rabi frequencies

$$\tilde{\Omega}_{ij}(x) = \tilde{\Omega}_{ij} \cos(\tilde{K}_0 x), \quad (\text{C2})$$

The adiabatic elimination of the electronic excited levels leads to the AC stark shift

$$H_{\text{int}} = [\tilde{\Delta}_1 |g_1\rangle \langle g_1| + \tilde{\Delta}_2 |g_2\rangle \langle g_2|] \cos^2(\tilde{K}_0 x), \quad (\text{C3})$$

where

$$\begin{aligned} \tilde{\Delta}_1 &= \frac{|\tilde{\Omega}_{\tilde{e}_1 g_1}|^2}{4(\tilde{\omega}_{\text{sw}} - \tilde{\omega}_1)}, \\ \tilde{\Delta}_2 &= \frac{1}{4} \left(\frac{|\tilde{\Omega}_{e_1 g_2}|^2}{\tilde{\omega}_{\text{sw}} + \omega_Z - \omega_1} + \frac{|\tilde{\Omega}_{\tilde{e}_2 g_2}|^2}{\tilde{\omega}_{\text{sw}} + \omega_Z - \tilde{\omega}_2} \right). \end{aligned} \quad (\text{C4})$$

Since $\tilde{\Delta}_1 \tilde{\eta}^2, \tilde{\Delta}_2 \tilde{\eta}^2 \ll |\Omega_y|$ ($\tilde{\eta} = \tilde{K}_0 \ell_x < 1$ is the Lamb-Dicke parameter), we can project H_{int} onto the ground state $|\downarrow\rangle_x$ of σ_x , and obtain

$$H_{\text{int}} = \Omega_{\text{int}} \cos^2(\tilde{K}_0 r_x), \quad (\text{C5})$$

where $\tilde{K}_0 d = 4\pi n$ (n is an integer), Ω_{int} is the effective Rabi frequency. By assuming that the center of the microtrap is at the anti-node of the standing wave and expanding the cosine term in H_{int} , we obtain the phonon-phonon interaction

$$H_U = U_{\text{int}} a_x^{\dagger 2} a_x^2, \quad (\text{C6})$$

where we have neglected the phonon number non-conserving terms. Notice that the second order in r_x just renormalizes the trap frequency, and can be absorbed in $\tilde{\omega}_x$. Here, the on-site interaction $U_{\text{int}} = 2\Omega_{\text{int}} \tilde{\eta}^4$ can be tuned by the external laser beams.

-
- [1] I. Bloch, J. Dalibard, and W. Zwerger, *Rev. Mod. Phys.* **80**, 885 (2008).
- [2] M. Lewenstein, A. Sanpera, and V. Ahufinger, *Ultracold Atoms in Optical Lattices: Simulating quantum many-body systems* (Oxford University Press, 2012).
- [3] D. Jaksch, C. Bruder, J. I. Cirac, C. W. Gardiner, and P. Zoller, *Phys. Rev. Lett.* **81**, 3108 (1998).
- [4] W. Hofstetter, J. I. Cirac, P. Zoller, E. Demler, and M. D. Lukin, *Phys. Rev. Lett.* **89**, 220407 (2002).
- [5] M. Greiner, O. Mandel, T. Esslinger, T.W. Hänsch, and I. Bloch, *Nature* **415**, 39 (2002).
- [6] J. F. Sherson, C. Weitenberg, M. Endres, M. Cheneau, I. Bloch, and S. Kuhr, *Nature* **467**, 68 (2010); C. Weitenberg, M. Endres, J. F. Sherson, M. Cheneau, P. Schauß, T. Fukuhara, I. Bloch, and S. Kuhr, *Nature* **471**, 319 (2011).
- [7] W. S. Bakr, A. Peng, M. E. Tai, R. Ma, J. Simon, J. Gillen, S. Foelling, L. Pollet, and M. Greiner, *Science* **329**, 547 (2010); W. S. Bakr, J. I. Gillen, A. Peng, S. Foelling, and M. Greiner, *Nature* **462**, 74 (2009).
- [8] D. Porras and J. I. Cirac, *Phys. Rev. Lett.* **93**, 263602 (2004).
- [9] D. Porras and J. I. Cirac, *Phys. Rev. Lett.* **92**, 207901 (2004); X. L. Deng, D. Porras, and J. I. Cirac, *Phys. Rev. A* **72**, 063407 (2005). K. Kim, M. S. Chang, R. Islam, S. Korenblit, L. M. Duan, and C. Monroe, *Phys. Rev. Lett.* **103**, 120502 (2009).
- [10] see R. Blatt and C. F. Roos, *Nat. Phys.* **8**, 277 (2012) and references therein.
- [11] A. Friedenauer, H. Schmitz, J. T. Glueckert, D. Porras and T. Schätz, *Nat. Phys.* **4**, 757 (2008); Ch. Schneider, M. Enderlein, T. Huber and T. Schätz, *Nat. Photon.* **4**, 772 (2010); K. Kim, M. S. Chang, S. Korenblit, R. Islam, E. E. Edwards, J. K. Freericks, G. D. Lin, L. M. Duan, and C. Monroe, *Nature* **465**, 590 (2010); R. Islam, E. E. Edwards, K. Kim, S. Korenblit, C. Noh, H. Carmichael, G. D. Lin, L. M. Duan, C. C. J. Wang, J. K. Freericks, and C. Monroe, *Nat. Commun.* **2**, 377 (2011); B. P. Lanyon, C. Hempel, D. Nigg, M. Müller, R. Gerritsma, F. Zähringer, P. Schindler, J. T. Barreiro, M. Rambach, G. Kirchmair, M. Hennrich, P. Zoller, R. Blatt, and C. F. Roos, *Science* **7**, 57 (2011).
- [12] J. Chiaverini, R. B. Blakestad, J. Britton, J. D. Jost, C. Langer, D. Leibfried, R. Ozeri, and D. J. Wineland, *Quant. Inf. Comput.* **5**, 419 (2005).
- [13] R. Schmied, J. H. Wesenberg, and D. Leibfried, *Phys. Rev. Lett.* **102**, 233002 (2009).
- [14] J. T. Merrill, C. Volin, D. Landgren, J. M. Amini, K. Wright, S. C. Doret, C. S. Pai, H. Hayden, T. Killian, D. Faircloth, K. R. Brown, A. W. Harter, and R. E. Slusher, *New J. Phys.* **13**, 103005 (2011).
- [15] S. X. Wang, J. Labaziewicz, Y. Ge, R. Shewmon, and I. L. Chuang, *Phys. Rev. A* **81**, 062332 (2010); T. H. Kim, P. F. Herskind, T. Kim, J. Kim, and I. L. Chuang, *Phys. Rev. A* **82**, 043412 (2010); R. J. Clark, Z. Lin, K. S. Diab, and I. L. Chuang, arXiv:1009.0036; T. H. Kim, P. F. Herskind, and I. L. Chuang, *Appl. Phys. Lett.* **98**, 214103 (2011).
- [16] A. Ozakin and F. Shaikh, arXiv:1109.2160; D. L. Moehring, C. Highstrete, D. Stick, K. M. Fortier, R. Haltli, C. Tigges, and M. G. Blain, *New J. Phys.* **13**, 075018 (2011).
- [17] R. Schmied, T. Roscilde, V. Murg, D. Porras, and J. I. Cirac, *New J. Phys.* **10**, 045017 (2008).
- [18] F. D. M. Haldane, *Phys. Rev. Lett.* **61**, 2015 (1988).
- [19] K. Sun, Z. Gu, H. Katsura, and S. Das Sarma, *Phys. Rev. Lett.* **106**, 236803. (2011); E. Tang, J. W. Mei, and X. G. Wen, *Phys. Rev. Lett.* **106**, 236802 (2011); T. Neupert, L. Santos, C. Chamon, and C. Mudry, *Phys. Rev. Lett.* **106**, 236804 (2011); Y. Wang, H. Yao, Z. Gu, C. D. Gong, and D. N. Sheng, *Phys. Rev. Lett.* **108**, 126805 (2012). S. Yang, Z. C. Gu, K. Sun, and S. Das Sarma, arXiv:1205.5792.
- [20] X. L. Qi, T. L. Hughes, and S. C. Zhang, *Phys. Rev. B* **78**, 195424 (2008).
- [21] F. D. M. Haldane and S. Raghu, *Phys. Rev. Lett.* **100**, 013904 (2008); *Phys. Rev. A* **78**, 033834 (2008).
- [22] N. Y. Yao, C. R. Laumann, A. V. Gorshkov, H. Weimer, L. Jiang, J. I. Cirac, P. Zoller, and M. D. Lukin, arXiv:1110.3788.
- [23] N. R. Cooper, N. K. Wilkin and J. M. F. Gunn, *Phys. Rev. Lett.* **87**, 120405 (2001).
- [24] R. Dum and M. Olshanii, *Phys. Rev. Lett.* **76**, 1788 (1996).
- [25] Y. J. Lin, R. L. Compton, A. R. Perry, W. D. Phillips, J. V. Porto, and I. B. Spielman, *Phys. Rev. Lett.* **102**, 130401 (2009).
- [26] J. Dalibard, F. Gerbier, G. Juzeliūnas, and P. Öhberg, *Rev. Mod. Phys.* **83**, 1523 (2011).
- [27] D. Jaksch and P. Zoller, *New J. Phys.* **5**, 56 (2003).
- [28] M. Hafezi, A. S. Sørensen, E. Demler, and M. D. Lukin, *Phys. Rev. A* **76**, 023613 (2007).
- [29] N. R. Cooper, E. H. Rezayi and S. H. Simon, *Phys. Rev. Lett.* **95**, 200402 (2005).
- [30] S. G. Bhongale, L. Mathey, S. W. Tsai, C. W. Clark, and E. Zhao, *Phys. Rev. Lett.* **108**, 145301 (2012).
- [31] B. C. Sansone, C. Trefzger, M. Lewenstein, P. Zoller, and G. Pupillo, *Phys. Rev. Lett.* **104**, 125301 (2010); C. Menotti, C. Trefzger, and M. Lewenstein, *Phys. Rev. Lett.* **98**, 235301 (2007).
- [32] N. Y. Yao, C. R. Laumann, A. V. Gorshkov, S. D. Bennett, E. Demler, P. Zoller, and M. D. Lukin, arXiv:1207.4479.
- [33] A. Bermudez, T. Schaetz, and D. Porras, *Phys. Rev. Lett.* **107**, 150501, (2011).
- [34] K. Fang, Z. Yu, and S. Fan, *Phys. Rev. B* **84**, 075477 (2011).
- [35] Since we are using a Raman transition (see Appendix A), the Lamb-Dicke parameter is a factor 2 larger than the standard one.
- [36] G.E. Volovik, *The Universe in a Helium Droplet* (Clarendon, Oxford, 2003).
- [37] D. Xiao, M. Chang, and Q. Niu, *Rev. Mod. Phys.* **82**, 1959 (2010).
- [38] T. T. Wu and C. N. Yang, *Phys. Rev. D* **12**, 3845 (1975).
- [39] D. J. Thouless, M. Kohmoto, M. P. Nightingale, and M. den Nijs, *Phys. Rev. Lett.* **49**, 405 (1982).
- [40] V. M. Stojanovic, T. Shi, C. Bruder, and J. I. Cirac, arXiv:1206.7010.
- [41] B. Horstmann, B. Reznik, S. Fagnocchi, and J. I. Cirac, *Phys. Rev. Lett.* **104**, 250403 (2010); B. Horstmann, R. Schützhold, B. Reznik, S. Fagnocchi, and J. I. Cirac, *New*

- J. Phys. **13**, 045008 (2011).
- [42] H. Fröhlich, Proc. Roy. Soc. A **215**, 291 (1952).